CHEMICAL PHYSICS

Diffusiophoresis-enhanced Turing patterns

Benjamin M. Alessio and Ankur Gupta*

Turing patterns are fundamental in biophysics, emerging from short-range activation and long-range inhibition processes. However, their paradigm is based on diffusive transport processes that yield patterns with shallower gradients than those observed in nature. A complete physical description of this discrepancy remains unknown. We propose a solution to this phenomenon by investigating the role of diffusiophoresis, which is the propulsion of colloids by a chemical gradient, in Turing patterns. Diffusiophoresis enables robust patterning of colloidal particles with substantially finer length scales than the accompanying chemical Turing patterns. A scaling analysis and a comparison to recent experiments indicate that chromatophores, ubiquitous in biological pattern formation, are likely diffusiophoretic and the colloidal Péclet number controls the pattern enhancement. This discovery suggests that important features of biological pattern formation can be explained with a universal mechanism that is quantified straightforwardly from the fundamental physics of colloids.

INTRODUCTION

In his seminal paper, Alan Turing proposed that reaction-diffusion instabilities could give rise to pattern formation in biological systems, a phenomenon now known as Turing patterns (*1*). Subsequent research has provided experimental evidence for the existence of Turing patterns in a variety of biological contexts, including zebrafish embryogenesis (*2*), hair follicle spacing (*3*), emulsion-based chemical cells (*4*), patterns found on zebrafish through cell-cell interactions (*5*), and the development of fingers from early limb buds (*6*). Theoretical advances have led to the development of modifications to Turing's original model (*7*), including the widely used Gierer-Meinhardt (*8*), Brusselator (*9*, *10*), and cell-cell interaction (*5*) models. These models and their derivatives have been used to reproduce a wide range of patterns found in nature (*11*), from the wave-like patterns on marine angelfish (*12*) to the stripe-like patterns on zebrafish (*5*, *13*) and even patterns on sea shells (*14*). However, these models typically rely on diffusive transport mechanisms to generate concentration gradients, suffer from poor robustness owing to many complicated factors (*15*), and have thus far neglected the role of convective transport. We propose that, in the context of Turing patterns, cells convect and steepen using diffusiophoresis, which is the propulsion of colloids by a chemical gradient. This mechanism promotes the color sharpening that is observed in nature and improves the robustness of the models by introducing an independent control parameter for this sharpness.

Previous attempts to replicate the sharp gradients observed in natural Turing patterns have prescribed ad hoc mechanisms including inflated drift terms (*16*), switching systems (*7*), and reaction pathway coupling (*17*). However, a complete physical justification for such processes remains elusive. A more natural mechanism to obtain sharp gradients in concentration comes from operating in the regime of high Péclet numbers, i.e., conditions where the convective transport dominates the diffusive transport. This regime might appear to be difficult to obtain in the absence of fluid flow. However, such a regime is commonly observed in microfluidic experiments with colloidal particles via the process of diffusiophoresis, i.e., transport of colloidal particles in response to solute concentration gradients (*18*–*30*). The key feature observed in diffusiophoretic systems is the banding of colloidal particles that creates a region of sharp colloidal concentration gradients (*18*, *21*, *25*, *26*, *29*–*31*). The diffusiophoretic transport of colloids, which has been seen to occur with a Péclet number $\mathrm{Pe} = O(10) - O(10^3)$ (the ratio of particle convective flux to diffusive flux) (*18*, *25*, *30*, *29*), creates these banded structures that can be further enhanced in the presence of acid-base reactions (*20*). We note that chemotaxis can be qualitatively similar to diffusiophoresis and has been proposed in the past (*32*) as an explanation for subtle features arising from time-dependent processes in the development of angelfish. Such an effect has, however, been neglected in more recent state-of-the-art explanations of chromatophore pattern formation (*5*, *33*). As we will argue, chromatophores are likely diffusiophoretic. As discovered experimentally by Ramm *et al.* (*34*), diffusiophoresis plays an important role for biological pattern formation even in the absence of chemotaxis, as it is a more fundamental and robust physical phenomenon that does not rely on cellular sensing. Thus, any model of biological pattern formation should include diffusiophoresis, if not also chemotaxis, and by doing so, one can promote robustness and recover essential features not well captured by the state-of-the-art models.

Over the past decade, several studies have concluded that diffusiophoresis is a key process that was previously overlooked. For instance, Florea *et al.* (*35*) elucidated, both theoretically and experimentally, that diffusiophoresis is responsible for creating an exclusion zone near charged surfaces and stated that diffusiophoresis is "likely to play an important, yet unexplored role" in biological processes. Similarly, Shin *et al.* (*36*) underscored the role of diffusiophoresis in removing contaminants from porous, fibrous materials in the presence of surfactant concentration gradients. Therefore, we surmise that diffusiophoresis of chromatophores could play an important role in the process of biological pattern formation.

Some of the most readily observable Turing patterns are animal skin patterns. Our central argument is that during biological pattern formation, chromatophores, which are specialized pigment cells known to control the coloration pattern on fish (*37*), respond diffusiophoretically to physiological reactions. There are different

Department of Chemical and Biological Engineering, University of Colorado, Boulder, CO, USA.
*Corresponding author. Email: ankur.gupta@colorado.edu

types of chromatophores, including melanophores, xanthophores, erythrophores, iridophores, and leucophores (*38*), which are organized in multiple layers and can interact with each other to create complex, even regenerative or adaptive patterns (*39*, *40*). We postulate that chromatophores are diffusiophoretic because of three primary reasons. First, the size of a typical chromatophore can range from 1 to 30 μm, which is typically the range where colloidal particles are diffusiophoretic (*41*, *42*). Second, recent experimental results suggest that chromatophores are charged and interact with the surrounding medium (*43*). Last, the biological reactions in the surrounding medium can create concentration gradients of small molecules that will interact with the chromatophore; multicomponent physiological reactions have been known to control chromatophore aggregation and dispersion (*44*). We also emphasize that diffusiophoresis of chromatophore-coated particles has been experimentally reported in literature (*43*). In a biological setting, we expect that particle motion is made complex by effects such as cell-cell adhesion and resistance of the porous membrane. Regardless, such effects do not affect the essential physics leading to steepening.

RESULTS

We consider a dilute mixture of two different types of species: small-molecule solutes and microscale colloids. The concentration of small molecules is denoted by c_i, where $i \in [1, S_C]$ such that S_C is the total number of solute molecule species. The concentration of colloids are given by n_j, where $j \in [1, S_N]$ such that S_N is the total number of microparticle species. The transport equation of solutes and colloids, assuming dilute suspensions absent of steric effects, are given by

$$\frac{\partial c_i}{\partial t} = D_{c_i}\tilde{\nabla}^2 c_i + R_{c_i} \tag{1A}$$

$$\frac{\partial n_j}{\partial t} + \tilde{\nabla}\cdot(\mathbf{v}_{\mathrm{DP}j} n_j) = D_{n_j}\tilde{\nabla}^2 n_j \tag{1B}$$

where t is time and D_{c_i} and D_{n_j} are the diffusivities of the ith solute and the jth colloid, respectively. R_{c_i} is the production rate of the ith solute. The term $\mathbf{v}_{\mathrm{DP}j} = \sum_i m_{ij}\tilde{\nabla}c_i$ represents the induced diffusiophoretic velocity of the jth colloid due to the concentration gradients of solutes, proportional to the diffusiophoretic mobility coefficient m_{ij}. For simplicity, we use the nonelectrolyte form of $\mathbf{v}_{\mathrm{DP}}$ (*31*), but more complicated forms are well described in the literature (*45*, *30*). There is no background fluid flow, although realistic experimental settings are expected to have a strong influence of background flow originating from the solute-geometry interactions (*30*, *29*). We note that the sign of the divergence in Eq. 1B affects the shape of the steepening pattern (see the "Analytical model" section). Before proceeding further, we introduce nondimensional quantities where $C_i = c_i/c^\star$, $N_i = n_i/n^\star$, $T = tD_{c_1}/\ell^2$, $\mathscr{D}_C = D_{c_i}/D_{c_1}$, $\mathscr{D}_{N_i} = D_{n_i}/D_{C_1}$, $\mathscr{R}_{C_i} = R_{c_i}/D_{c_i}/c^\star\ell^2$, $\mathbf{V}_{\mathrm{DP}j} = \mathbf{v}_{\mathrm{DP}j}\ell/D_{c_1}$, and $\nabla = \ell\tilde{\nabla}$, where $c^\star$ and $n^\star$ are reference concentrations for solute and colloids, respectively, ℓ is a reference length scale, and D_{c_1} is the diffusivity of the first solute. These substitutions yield the equations

$$\frac{\partial C_i}{\partial T} = \mathscr{D}_{C_i}\nabla^2 C_i + \mathscr{R}_{C_i} \tag{2A}$$

$$\frac{\partial N_j}{\partial T} + \nabla\cdot(\mathbf{V}_{\mathrm{DP}_j} N_j) = \mathscr{D}_{N_j}\nabla^2 N_j \tag{2B}$$

To induce Turing patterns, we define a four-component model with two solute species and two chromatophore species. We use the Brusselator model for solute species to describe the reaction and production rates that are given by (*9*, *10*)

$$\mathscr{R}_{C_1} = \mathrm{Da}_C[A - (B+1)C_1 + C_1^2 C_2] \tag{3A}$$

$$\mathscr{R}_{C_2} = \mathrm{Da}_C(BC_1 - C_1^2 C_2) \tag{3B}$$

A and B are scaled concentrations of excess components [see (*46*) for details], $\mathrm{Da}_C = k\ell^2/D_{c_1}$ is Damköhler number for the solutes, and k is the first-order reaction constant. We define diffusiophoretic velocities for the two colloids as follows

$$\mathbf{V}_{\mathrm{DP}_1} = M_{11}\nabla C_1 + M_{21}\nabla C_2 \tag{4A}$$

$$\mathbf{V}_{\mathrm{DP}_2} = M_{12}\nabla C_1 + M_{22}\nabla C_2 \tag{4B}$$

where M_{11}, M_{21}, M_{12}, and M_{22} are diffusiophoretic mobility coefficients. We note that for electrolytic diffusiophoresis, the dependence of diffusiophoretic velocity is with the gradient of the log of the concentrations (*28*, *41*). However, because the exact nature of interactions between solute and biological colloids remain unknown (*47*), for simplicity, we use the relationship for nonelectrolytic interactions (*31*). We note that the values of mobility coefficients are related to Péclet number Pe (which is mathematically defined in Eq. 5) and are typically at most $O(1)$. A detailed mathematical treatment of the Péclet number is included later in the results section of this manuscript. We solve Eqs. 2A and 2B with initial conditions of unit concentrations and no-flux boundary conditions. The details of numerical simulations are provided in the "Numerical simulations" section.

The minimum mathematical model that qualitatively reproduces the features of biological patterns consists of two reactive-diffusive species that interact with each other through a nonlinear reaction mechanism (*1*, *8*–*10*, *12*, *13*). The most natural interpretation, as assumed in state-of-the-art models (*13*) is to assume that these two species are chromatophores. We demonstrate here how this assumption limits the patterns to be less sharp than those observed in nature. Comparing the natural patterns observed in ornate boxfish (*Aracana ornata*) with the Brusselator model (Eq. 3A, where C_1 and C_2 are replaced by N_1 and N_2, D_{C_i} is replaced by D_{N_i}, $\mathscr{R}_{C_1}$ and $\mathscr{R}_{C_2}$ are changed to $\mathscr{R}_{N_1}$ and $\mathscr{R}_{N_2}$, and Da_C is modified to Da_N), assuming a blue and a yellow chromatophore to be our reactive species, as observed in Fig. 1, the Brusselator model is able to reproduce the patterns of hexagon and stripes seen in the boxfish but is unable to capture the sharpness of color gradients observed in the fish. Besides the size of the fish, in the natural fish patterns, there are two distinct length scales (see the "Scaling arguments" section). For instance, for the hexagon pattern, there is a clear length scale separation between the edge thickness, ℓ_t, and the length of the

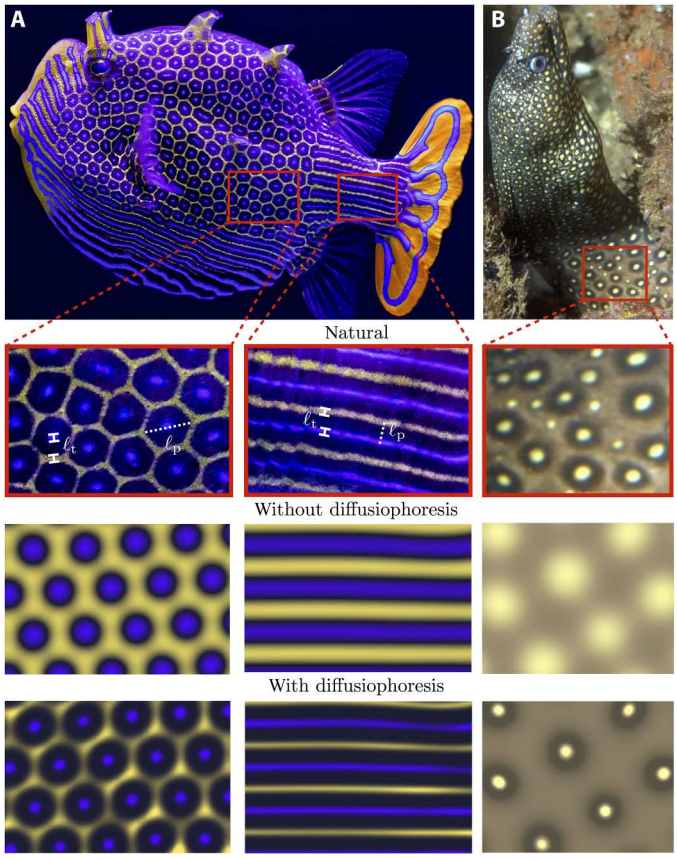

Fig. 1. Comparison of natural patterns in fish simulations. (**A**) A male ornate boxfish (*A. ornata*) has intricate hexagon and stripe patterns on its skin. Reaction-diffusion models can capture the nature of the pattern but are unable to reproduce the sharpness of the color gradients. Instead, diffusiophoresis-enhanced reaction-diffusion shows a notable resemblance to the natural patterns when compared to simulations from our model. Photo courtesy of the Birch Aquarium at the Scripps Institution of Oceanography. White line segments and dashed lines indicate the edge thickness, i.e., ℓ_t and pattern sizes ℓ_p, respectively. (**B**) A jewel moray eel (*M. lentiginosa*). The double spot pattern cannot be reproduced from a two-component reaction-diffusion dynamics alone but is easily simulated as a diffusiophoretic process. Image by craigjhowe, used under CC BY-NC 4.0 license. Source: iNaturalist observation 37252428.

hexagon pattern, ℓ_p. Similarly, for the stripe pattern, there is a distinction between the the thickness of the stripes ℓ_t and the separation between the stripes ℓ_p. The reaction-diffusion models have an inherent limitation that $\ell_t = \ell_p$, leading to a diffuse pattern formation. Accordingly, they are unable to recover double spot patterns such as those seen on the jewel moray eel (*Muraena lentiginosa*) unless multiple nonlinear reaction mechanisms are invoked, i.e., two or more Brusselators are coupled (*17*), which still yield a diffuse pattern unlike the ones observed in nature. We must look for mechanisms beyond the nonlinear reaction-diffusion interactions.

While experiments (*5*, *33*) have soundly implicated chromatophores in pattern formation in zebrafish skin, recent evidence (*5*) suggests that a third species, which is more diffusive and is thus a small molecule, is required for a more complete picture of the process. This invites the possibility of robust control of separate length scales, where ℓ_p is associated with the molecular substance (s) and ℓ_t is associated with the chromatophores. Furthermore, prior studies on two-component models used species diffusion coefficients $O(10^{-10}) - O(10^{-9})$ m^2/s to obtain patterns that resemble the ones observed in nature (*12*). These diffusivity values resemble small molecules instead of microparticles, which have diffusivities $O(10^{-13})$ m^2/s. Accordingly, we assert that there are two broad categories of species present in the system: molecular-scale solute species (i.e., morphogens or long-range mediators) and microscopic-scale colloidal species (i.e., chromatophores). This is supported by prior experiments (*44*) and has strong implications for the stability of Turing patterns in biological contexts. Recently, Pelz and Ward (*48*) discovered that for a theoretical framework with chemicals reacting on the surface of cells (or in compartments) and diffusing and degrading throughout an intercell medium, the diffusivity ratio required for stationary Turing patterns can be as low as unity given instead a reaction rate difference between the chemical species. Our proposed model extends their approach by considering the ever-present mechanical forces that act on cells under chemical gradients. To simplify the problem and isolate the physical effects of diffusiophoresis, we do not consider the cells to have any effect on the stability of the chemical patterns, which is a central feature to the work of Pelz and Ward and must be considered for a quantitatively accurate model.

The transport equations for two-component chromatophore models are primarily dependent on the Damköhler number of the colloids Da_N, which is the ratio of the diffusion time scale to the reaction time scale, where an increase in Da_N corresponds to a decrease in ℓ_p. However, in our proposed model that builds on the recent experimental findings (*5*), the reactions are driven by solutes, and the chromatophores respond to the concentration gradients of the solutes diffusiophoretically (Eqs. 2A and 4A). In this proposed setup, the two dimensionless groups that control the behavior of the patterns are the Damköhler number of the solute, Da_C, and the Péclet number of the colloids, Pe. Typically, $\mathrm{Pe} = O(10) - O(10^3)$ (*18*, *26*, *28*). Physically, we propose that transport of the solute molecules sets only the pattern type and size ℓ_p, whereas the diffusiophoretic transport of colloids dictates only the thickness ℓ_t. The length scales that we are dealing with will change considerably in many natural systems, for example, as a fish grows from a baby to an adult, in ways that considerably alter pattern formation because of confinement (*15*, *32*). This growth can be represented by a velocity term, which we do not include here, as it would not affect the essential features of our model.

Our proposed model is able to recover, to a considerable degree, the natural patterns of hexagons and stripes observed in the ornate boxfish and the double-spot pattern in the jewel moray eel using the Brusselator model with diffusiophoresis (see Fig. 1 and movies S1 and S2). While the reaction-diffusion model without diffusiophoresis produces qualitative features of the chromatophore patterns, by including diffusiophoresis, we capture the steepening effect. This feature is universal and not exclusive to the Brusselator model. In Fig. 2 and movies S3 and S4, we perform the same comparison between reaction-diffusion models with and without diffusiophoresis for both the Gierer-Meinhardt model (*8*) and cell-cell interaction model (see the "Numerical simulations" section for details) (*5*). In these models, just as with the Brusselator in Fig. 1, the sharpening effect of diffusiophoresis is apparent both in the finer length scales and the greater magnitude of depletion away from the hotspots (i.e.,

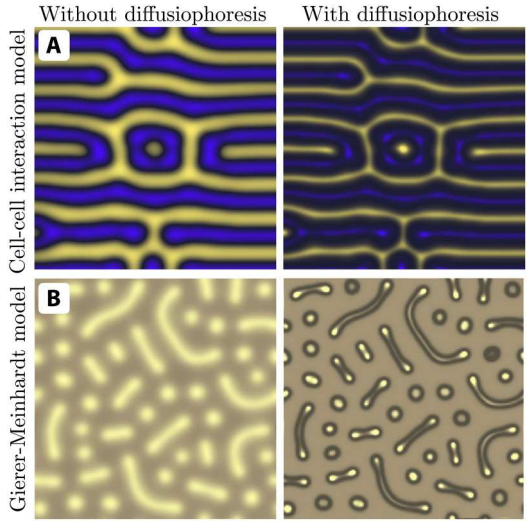

Fig. 2. Diffusiophoretic enhancement for various reaction-diffusion mechanisms. (**A**) Cell-cell interaction model (*5*). (**B**) Gierer-Meinhardt model (*8*). For both rows, the left panel shows a stable pattern arising from purely reactive-diffusive mechanisms, and the right panel shows the steepening effect of diffusiophoresis.

the color of the two phases is more distinct with the inclusion of diffusiophoresis). Because of its relative abundance and depth of analytical theory in the literature, here, we center our analysis on the Brusselator model, but the fundamental physics at play is agnostic to the model.

To further emphasize the distinction between the proposed and the reaction-diffusion mechanisms, in fig. S1, we compare the hexagon pattern for different values of Da_N in the reaction-diffusion model and different values of Pe in the proposed model. As is clear from the results, increasing Da_N simply decreases ℓ_p without changing the relative thickness of concentration gradients, i.e., ℓ_t/ℓ_p is constant. In contrast, an increase in Pe does not modify ℓ_p but reduces ℓ_t and better resembles the patterns observed in nature. In our simulations, we found strongest qualitative agreement with natural patterns when setting Pe in the range of 10 to 50. This is consistent with the effective Pe number observed in recent theoretical and experimental findings (*29*, *30*). We acknowledge that we neglect interparticle interactions and invoke the assumption of a dilute suspension, which, in some limits, may cause our simulations to underpredict values of ℓ_t.

Next, we focus on quantifying the pattern formation of chromatophores via diffusiophoresis. For simplicity, we focus on the Brusselator model for solute reactions (fig. S2A), although our analysis is readily extended to other reaction-diffusion frameworks (*13*). In the Brusselator model (*9*, *10*), two abundant reactants with concentrations A and B produce solutes with concentrations C_1 and C_2, where concentrations are scaled by $c^\star$. An initially homogeneous state of C_1 and C_2 can spontaneously come into formation when perturbations of permitted wavelengths grow into patterns such as hexagons or stripes; the resulting gradients ∇C_1 and ∇C_2 generate the diffusiophoretic velocity $V_{DP_j} = M_{j1} \nabla C_1 + M_{j2} \nabla C_2$ of the colloid (i.e., chromatophore) for diffusiophoretic mobility M_i corresponding to C_i, where M_{ji} is the dimensionless diffusiophoretic mobility that induces the velocity in the jth colloid because of the ith solute. The results in fig. S2 highlight that two different diffusiophoretic colloids with different mobilities, denoted with white and red dots, mirror the pattern of the solute to form hexagons and stripes but produce sharper and more well-defined features than the solute alone. Only concentration hotspots of C_1 are shown (in green) because the concentration distribution of C_2 has the same spatial structure as C_1. Here, we further reduce the parameter space by focusing on a system with one colloid only, and therefore, we drop the jth subscript in M_{ji} and refer to it as M_i.

By using the framework of amplitude equations, we analytically predict solute and relative colloid concentrations for different patterns produced with the Brusselator model, including an analytical expression for the steepening ratio λ_N/λ_C. Theoretical investigations of the Brusselator model (*46*) have revealed a complex parameter

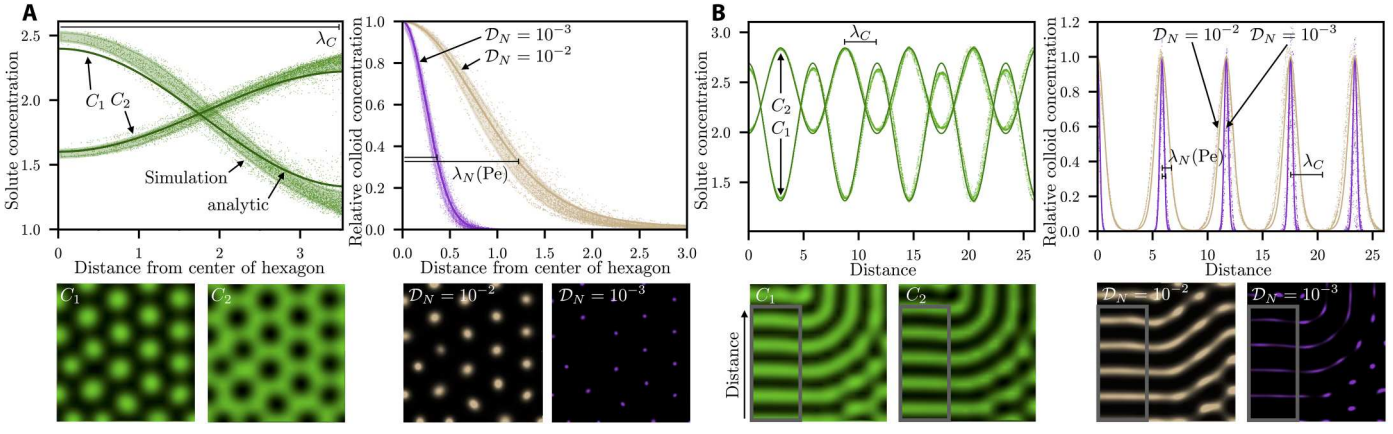

Fig. 3. Controlling the edge thickness of Brusselator patterns. (**A**) Comparison of analytically derived and numerically computed forms of (left) solutes and (right) colloidal concentration profiles, averaged radially over all hexagons in the frame. The solute concentrations are simulated with parameters $\mu = 0.05$, $A = 1.5$, and $\mathscr{D}_{C_2} = 4$. The colloidal concentrations correspond to two different simulations $\mathscr{D}_N = 10^{-2}$ and $\mathscr{D}_N = 10^{-3}$, migrating with $M_1 = M_2 = 0.1$ for both cases. Solute and colloidal length scales are indicated with line segments. The shading in all curves represents 1 SD of the numerical data points. (**B**) Comparison of analytically derived and numerically computed forms of (left) solutes and (right) colloidal concentration profiles with vertical distance, averaged across the stripes in the gray boxes. The solute concentrations are simulated with parameters $\mu = 0.04$, $A = 2$, and $\mathscr{D}_{C_2} = 3$. The colloidal concentrations correspond to two different simulations $\mathscr{D}_N = 10^{-2}$ and $\mathscr{D}_N = 10^{-3}$, migrating with $M_1 = M_2 = 0.1$ for both cases. Solute and colloidal length scales are indicated with line segments.

space where different Turing patterns form. The perturbations are sinusoidal in nature and have amplitudes that obey complex partial differential equations that encode the stability and form of these structures. Note that these amplitude equations do not predict two-dimensional (2D) or 3D patterns exactly but merely describe the size, shape, and stability of all possible structures; to simulate complete patterns, one must directly solve the system of reaction-diffusion equations, which are themselves sensitively dependent on initial conditions (*11*).

One of the dominant patterns in the Brusselator model is hexagonal arrays. Simulating stable hexagon patterns, in Fig. 3A, we plot the dependence of solute (left) and colloidal (right) concentrations with distance away from the center of the hexagon (averaged over all hexagons in the simulation box). The other dominant pattern in the Brusselator model is stripes, which we investigate in Fig. 3B. The solute (left) and colloidal (right) concentrations here are plotted along the periodic direction.

There are two length scales in each of the patterns described in Fig. 3. In hexagons, it is the size of the hexagons and the edge thickness of the hexagons. For stripes, it is the spacing between the stripes and the thickness of the stripes. The size of the hexagons and the spacing between the stripes is set by λ_C, i.e., the wavelength of the solute patterns, and the thickness of hexagons and stripes is set by λ_N. Crucially, the ratio of λ_N/λ_C is set by the Péclet number of the colloid for both the patterns. To explore this effect in more detail, we mathematically derive (see the "Analytical model" section) the Péclet number as

$$\mathrm{Pe} = \left| \frac{\alpha \left[M_1 - M_2 \frac{\eta(1+A\eta)}{A} \right]}{\mathscr{D}_N} \right| \tag{5}$$

where α is the amplitude of the perturbations to C_1 and $\eta = \mathscr{D}_{C_2}^{-1/2}$. We note that Eq. 5 is valid for both hexagon and stripe patterns. In the Brusselator model, the nondimensional solute concentration local to hexagon or stripe structures as a function of distance R from the local maximum is given by

$$C_i(R) = \sigma_i \alpha \cos\left(2\pi \frac{R}{\lambda_C}\right) + \text{const} \tag{6}$$

where we note that the 1D form of Eq. 6 is exact in the direction of maximal gradient for stripes and approximate for radially averaged hexagons. From the gradient of Eq. 6, we calculate the diffusiophoretic velocity

$$V_{\mathrm{DP}} = -\frac{2\pi}{\lambda_C}\alpha \left[M_1 - \frac{\eta(1+A\eta)}{A} M_2 \right] \sin\left(2\pi \frac{R}{\lambda_C}\right) \tag{7}$$

and the form of the steady-state colloid concentration

$$N(R) \propto \exp\left[\mathrm{Pe} \cos\left(2\pi \frac{R}{\lambda_C}\right) \right] \tag{8}$$

We define the colloid length-scale λ_N as the exponential decay distance, giving the analytical expression

$$\cos\left(2\pi \frac{\lambda_N}{\lambda_C}\right) = 1 - \frac{1}{\mathrm{Pe}} \tag{9}$$

See the "Analytical model" section for derivations. In Fig. 3, we show that our analytical model is in good quantitative agreement with simulation data extracted from a large number of both hexagons and stripes for solute and colloidal concentrations. We note that the analytical model has no discontinuities, and the colloid hotspots are predicted on a continuous and periodic curve.

It is clear from Eq. 9 that λ_N/λ_C can vary substantially through changes in Pe, revealing a control mechanism for the sharpness of Turing patterns involving colloidal particles. We further elucidate this control mechanism in Fig. 4 by comparing numerical predictions of λ_N/λ_C versus Pe to the analytical theory for the Brusselator model (Eq. 9). We obtain an approximately linear relationship between the two variables, consistent with our theoretical predictions, and show a collapse for two orders of magnitude of Pe. In the limit of low Pe, the steepening effect is diminished, and the colloid length scale approaches the solute length scale. If Pe is exactly zero, however, then there would be no mechanism for colloidal formation, and thus, λ_N/λ_C would be undefined.

In addition to the Brusselator model, we include, in Fig. 4, simulation data points for the Gierer-Meinhardt and the cell-cell interaction models. In the absence of an analytical prediction for the form of the solute field perturbations in these models, we estimate $\mathrm{Pe} = M/\mathscr{D}_N$, noting that we observe perturbation amplitudes of $\mathscr{O}(1)$ in our simulations. A more accurate representation of Péclet number would be the general form of Eq. 5, $\mathrm{Pe} = \sum_i \alpha_i M_i/\mathscr{D}_N$, where the sum is across each solute species and the coefficients α_i are dependent on the specific solute reaction-diffusion model. However, the analytical theory necessary to obtain such coefficients does not exist, to the best of our knowledge, for the Gierer-Meinhardt (*8*) and cell-cell (*5*) interaction models. Nonetheless, the data points from our simulations of these models are well-represented by a best-fit line, suggesting the collapse to a master curve of λ_N/λ_C versus Pe for models other than the Brusselator.

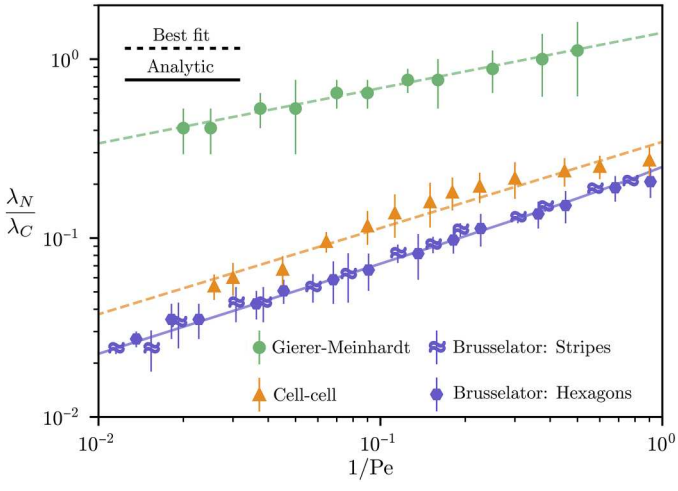

Fig. 4. Master curve of diffusiophoretic-enhanced Turing patterns. Comparison of simulation results with analytical predictions for the colloid hotspot length scale λ_N across a wide range of Péclet numbers. For the Brusselator model, hotspot length scales over both hexagon and stripe patterns are compared to an analytical curve with no fitting parameters. The same model parameters used in Fig. 3 are applied. For the Gierer-Meinhardt and cell-cell interaction models, data points are compared to a best-fit power law (see the "Numerical simulations" section for details). Error bars represent 1 SD in computations.

DISCUSSION

Our theory of diffusiophoretic sharpening of Turing patterns is strongly supported by recent experimental evidence (*34*). Ramm *et al.* discovered for pattern-forming MinDE protein systems in *Escherichia coli* that a purely diffusiophoretic mechanism induces replica patterns in colloidal species and, furthermore, that the patterns become sharper when the colloid size increases. This implies that as the Péclet number increases, the contrast between the two phases increases. The specific measurement of sharpness with which Ramm *et al.* quantify this effect is the Michelson intensity contrast: $(I_{max} - I_{min})/(I_{max} + I_{min})$. By using maximum and minimum colloidal concentration as a proxy for I_{max} and I_{min}, respectively, we demonstrate, using simulations of the Gierer-Meinhardt model, a similar trend to that observed experimentally by Ramm *et al.* of contrast versus colloid size (equivalently "cargo number"; see Fig. 5). We would like to emphasize that the Péclet numbers used in our simulations are only approximate, and thus, this comparison is qualitative. Nonetheless, this qualitative comparison is strong evidence that diffusiophoresis that sharpens Turing patterns is controlled by the Péclet number.

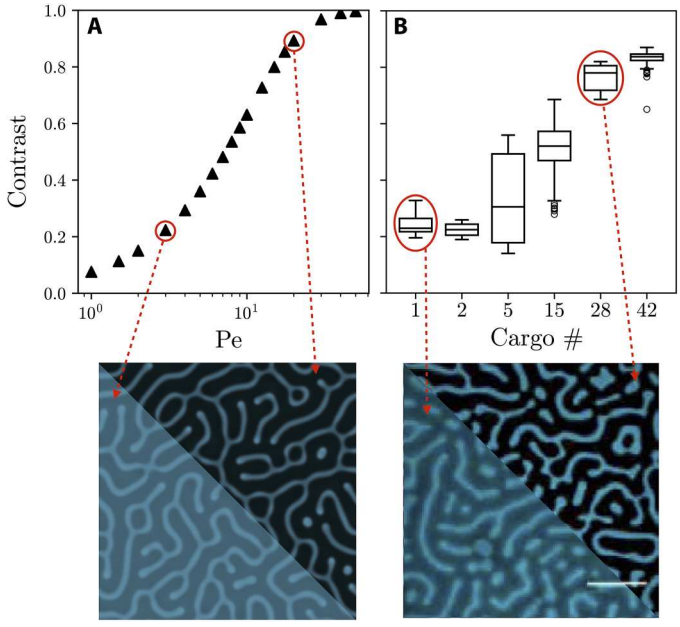

Fig. 5. Comparison between simulations and experiments. (**A**) We simulate colloidal patterns using the Gierer-Meinhardt model with varying colloidal Péclet number. The contrast in the simulation is defined as the ratio of the difference in maximum and minimum colloid concentration to the sum of maximum and minimum colloid concentration. The intensity contrast increases monotonically with the Péclet number, causing an *s*-like curve on the semi-log plot. (**B**) We compare to the experimental results obtained from Ramm *et al.* (*34*) (box plots were produced and experimental images were adapted by the authors using publicly available data via CC BY 4.0: https://creativecommons.org/licenses/by/4.0/legalcode). The contrast in experiments is defined as the ratio of the difference in maximum and minimum image intensity to the sum of maximum and minimum image intensity. An increase in cargo number is equivalent to an increase in Péclet number. Thus an increase in contrast with cargo number demonstrates that the simulations and experiments are in qualitative agreement with each other. The agreement is also notable in the intensity images (bottom), where the contrast strongly changes with Péclet number and cargo number. Red circles indicate specific data points whose corresponding images are shown.

The findings reported in this article open up numerous possibilities for future research and applications. For instance, further exploration of biological systems could reveal more instances where diffusiophoresis contributes to pattern formation such as embryo morphogenesis (*1*) and early life (*34*), which could subsequently lead to a better understanding of how these patterns emerge, evolve, and adapt in different species. In recent years, an embryonic framework has gained attention for understanding cancer ecosystems as chaotic expressions of the complex interactions between cellular and chemical components (*49*), and Turing patterns are theorized to play an important role in tumorigenesis (*50*). Unveiling diffusiophoresis as a mechanism in cellular organization processes can be crucial to future cancer research. Going forward, research might consider nonideal diffusion of the reacting species (*51*), complex colloidal interactions (*52*), dense packing effects (*53*), anisotropy (*54*), particle self-propulsion (*55*), liquid crystal order (*56*), and reaction-diffusion setups where cellular compartmentalization contributes to the chemical stability (*48*), which could reveal important control mechanisms of pattern formation in various biological systems. Experimental studies can observe the dynamics of the formation of Turing patterns with colloidal particles in controlled conditions. Beyond biophysics, understanding the role of diffusiophoresis in pattern formation has potential applications in engineering and materials science. By harnessing these mechanisms, researchers could develop methods for fabricating materials with precise microscale patterns (*16*). These materials could find applications in areas such as photonics, lab-on-a-chip devices, and biotechnology. In conclusion, our findings on the role of diffusiophoresis in pattern formation provide a foundation for future research and have the potential to affect a wide range of fields.

METHODS

Scaling arguments

Our numerical model relies on the following dimensionless groups: Da_C and Pe. To estimate Da_C, we recall that $Da_C = k\ell^2/D_{c_1}$. For small molecules, $D_{c_1} = O(10^{-10}) - O(10^{-9})$ m^2/s. On the basis of the typical experiments previously reported on fishes (*12*, *5*), it appears that $k = O(10^{-7}) - O(10^{-6})$ s^{-1}. We anticipate that this number can change for different kinds of fishes, and thus, this choice is the best estimate based on prior literature values. To determine an appropriate value of ℓ, we note that typical biological patterns have three main length scales. The simplest choice is to pick the size of an organism, which, for fishes, is typically $\ell_b = O(10^{-2}) - O(10^{-1})$ m. The second choice is the length scale of a repeating pattern (such as size of hexagon or the spacing between the stripes), which tends to be one order of magnitude smaller than the body size, or $\ell_p = O(10^{-3}) - O(10^{-2})$ m. Last, the third choice is the thickness of these patterns (see the thickness of the blue and yellow patterns on the fish in Fig. 1), which, at least for fishes, appears to be one order of magnitude smaller than ℓ_p, or $\ell_t = O(10^{-4}) - O(10^{-3})$ m. Out of these three choices, we postulate that ℓ_p is the most appropriate choice because $Da_C = O(1)$. This emphasizes the fact that the presence of small molecules is a crucial element for pattern formation. However, they only set the pattern size ℓ_p and not the pattern thickness ℓ_t, which we discuss next.

To estimate Pe, it is straightforward to see from Eq. 5 that $Pe = O(M/\mathscr{D}_N)$. As per prior literature values, $M \leq O(1)$ (*28*), and thus, Pe

$\leq O(1/\mathscr{D}_N)$. For a typical colloid, Pe = $O(10) - O(10^3)$. We note that recent findings have suggested that $\mathscr{D}_N$ is higher than the native diffusivity of the colloid due to dispersion, indicating a lower Pe than expected (*29*).

Analytical model

We restrict our analysis to chemical patterns exhibiting only critical wavelengths $\lambda_C = 2\pi/\sqrt{A\eta}$ (where $\eta = 1/\sqrt{\mathscr{D}_{C_2}}$), noting that this allows for a rich phase space while keeping our model simple (*46*). We consider solute concentrations that are 1D in distance R. These are exact in the direction of maximal gradient of stripe patterns and approximate for radially averaged hexagons. Setting $R = 0$ to be the location of the extremum, $\sigma_1 = 1$, $\sigma_2 = -\eta(1 + A\eta)/A$, and noting that the coefficient α depends on the pattern, we have Eq. 6. We define the supercriticality parameter $\mu \equiv (B - 1 - A\eta^2)/(1 + A\eta^2)$ and adapt the coefficients from the work of Peña and Pérez-García (*46*)

$$\alpha_{\text{stripes}} = \text{sign}(f)\sqrt{\mu/g} \tag{10A}$$

$$\alpha_{\text{hexagons}} = 3\frac{f + \text{sign}(f)\sqrt{f^2 + 4\mu(g + 2h)}}{2(g + 2h)} \tag{10B}$$

$$f = 2\frac{1 - A\eta}{A(1 + A\eta)} + \frac{2}{A}\mu \tag{10C}$$

$$g = \frac{-8 + 38A\eta + 5A^2\eta^2 - 8A^3\eta^3}{9A^3\eta(1 + A\eta)} \tag{10D}$$

$$h = \frac{-3 + 5A\eta + 7A^2\eta^2 - 3A^3\eta^3}{A^3\eta(1 + A\eta)} \tag{10E}$$

To determine the structure of the steady-state colloid concentration, we balance convection and diffusion

$$\frac{\partial}{\partial R}\left(D_N\frac{\partial N}{\partial R} - V_{\text{DP}}N\right) = 0 \tag{11}$$

where the diffusiophoretic velocity is given by Eq. 7. Requiring a bounded solution and defining the Péclet number as in Eq. 5, we get Eq. 8, which we compare to simulations in Fig. 3. We note that, depending on f, α can be positive or negative. In conjunction with the signs and magnitudes of M_1 and M_2, this property can flip the direction of V_{DP}. In the case of stripes, the sign change is trivially a phase shift. However, in the case of hexagons, our analytical model cannot accurately predict the length scale of the colloids, which are repulsed from the center, owing to complicated interactions with neighboring hexagons. In this case, one must rely on direct computation. For the same reason, our analysis cannot accurately predict any $\lambda_N > \lambda_C$. Last, our model can only tell us λ_N and not the maximum value of N; this value is sensitively dependent on early-time dynamics.

Numerical simulations

Our numerical calculations were implemented with the open-source partial differential equations solver Basilisk (*57*). We modified their multigrid solver of reaction-diffusion equations for the Brusselator model, which solves for C_1 and C_2, by including a diffusive tracer that is coupled in its advective term to ∇C_1 and ∇C_2. Basilisk's adaptive grid feature was used to retain accuracy at low colloid length scales; we required the solver to refine the grid to maintain an absolute accuracy of 0.1 in N (typically $\gg$1 at the local maxima). The minimum and maximum refinement levels were set to 5 and 12, respectively. The time steps were elected by the solver. In each of our simulations, we analyzed only the steady-state results; this was determined by inspection of simulation videos and time series of the domain maximum of N.

For all Brusselator simulations, we set $\ell_0 = 32\sqrt{k/D_{c_1}}$ and $\text{Da}_N = 1$ (except in fig. S1, we vary Da_N). For the hexagons (Figs. 1, 3A, and 4), we set $\mu = 0.05$, $A = 1.5$, and $D = 4$. For the stripes (Figs. 1, 3B, and 4), we set $\mu = 0.04$, $A = 2$, and $D = 3$. By keeping μ small, we observed chemical wavelengths approximately equal to their critical value, simplifying our analysis. The initial conditions are spatially homogeneous with $C_1 = A$ and $C_2 = \sqrt{1 + A\eta}(1 + \mu)/A + [\text{noise}]$, where the noise is uniformly sampled in between −0.01 and 0.01. This choice of initial condition for C_2 represents deviations of μ above the critical concentration of B, with the noise perturbing the initial homogeneity. The boundary conditions are no-flux. For the colloid, the initial condition is spatially homogeneous with $N = 1$, and no-flux boundary conditions are used. D_N, M_1, and M_2 are varied systematically.

For the simulations corresponding to both *A. ornata* and *M. lentiginosa*, we set the particle rates of diffusivity on the order of 10^{-4} relative to the solute, typical for micrometer-scale particles (*30*). To achieve control over the pattern thickness, we vary the diffusiophoretic mobilities relative to the solute rate of diffusivity between 2.5×10^{-2} and 10^{-1}. Although this is smaller than typical experimental values, to our knowledge, no experiments have been attempted to measure particle diffusiophoretic mobility in a biological membrane. Intuitively, we expect that this setting would permit diffusiophoretic mobilities much lower than those observed in microfluidic experiments. We also expect that the shape anisotropy of chromatophores reduces their diffusiophoretic mobility. Furthermore, we realize that colloidal dense packing effects might play an important role in these systems owing to the steady-state chemical gradient; such effects would reduce the diffusiophoretic convection.

We refer the reader to (*5*) for the details of the cell-cell interaction model. We implemented this model using the reaction-diffusion module of Basilisk, used the exact same parameters as (*5*), and imposed a diffusiophoretic advection (using the advective tracer module of Basilisk) of low-diffusivity substances (chromatophores u and v) in response to the gradient of the high-diffusivity substance (w) with varying Péclet number. The two diffusiophoretic chromatophores are assigned equal and opposite mobilities. In Fig. 2, we use 2D sinusoidal initial conditions with the observed wavelength and an overriding white noise field in the center, mimicking the pattern-forcing technique from (*5*). The same time step, box size, and adaptive grid technique as the Brusselator model implementation was applied. In Fig. 4, we impose purely 2D sinusoidal initial conditions of a stable wavelength to simplify our length scale analysis.

We refer the reader to (*58*) for a thorough implementation of the Gierer-Meinhardt model (*8*). Using the reaction-diffusion module of Basilisk, we implemented this model with the same parameters

and initial conditions as (*58*), electing $S = 0.55$, and used Basilisk's advective tracer module to calculate the diffusiophoretic response of a third, nonreactive substance of varying Péclet number. The same time step, box size, and adaptive grid technique as the Brusselator model implementation were applied.

Postprocessing was performed in Python 3.9, using NumPy, SciPy, and Matplotlib. The irregularly spaced output data were interpolated onto a 0.04×0.04 square grid using griddata from the scipy.interpolate package. Custom color maps were constructed using LinearSegmentedColormap from the matplotlib.colors package. Calculations of λ_N were performed by identifying the locations (in two dimensions for hexagons and in the 1D average for striped regions) of the maxima in colloid concentration using the peak_local_max function from the skimage.feature package, histogramming the data points to obtain relative colloid concentration as a function of radial distance from the maximum, and identifying the exponential decay distance for the average curve. Error was calculated by identifying the decay distances after adding and subtracting 1 SD to the average curve.

Supplementary Materials

This PDF file includes:
Figs. S1 and S2
Legends for movies S1 to S4

Other Supplementary Material for this manuscript includes the following:
Movies S1 to S4

REFERENCES AND NOTES

1. A. M. Turing, The chemical basis of morphogenesis. *Philos. Trans. R. Soc. London* **327**, 37–72 (1952).
2. P. Müller, K. W. Rogers, B. M. Jordan, J. S. Lee, D. Robson, S. Ramanathan, A. F. Schier, Differential diffusivity of Nodal and Lefty underlies a reaction-diffusion patterning system. *Science* **336**, 721–724 (2012).
3. S. Sick, S. Reinker, J. Timmer, T. Schlake, WNT and DKK determine hair follicle spacing through a reaction-diffusion mechanism. *Science* **314**, 1447–1450 (2006).
4. N. Tompkins, N. Li, C. Girabawe, M. Heymann, G. B. Ermentrout, I. R. Epstein, S. Fraden, Testing Turing's theory of morphogenesis in chemical cells. *Proc. Natl. Acad. Sci.* **111**, 4397–4402 (2014).
5. A. Nakamasu, G. Takahashi, A. Kanbe, S. Kondo, Interactions between zebrafish pigment cells responsible for the generation of Turing patterns. *Proc. Natl. Acad. Sci.* **106**, 8429–8434 (2009).
6. J. Raspopovic, L. Marcon, L. Russo, J. Sharpe, Digit patterning is controlled by a Bmp-Sox9-Wnt Turing network modulated by morphogen gradients. *Science* **345**, 566–570 (2014).
7. A. Koch, H. Meinhardt, Biological pattern formation: from basic mechanisms to complex structures. *Rev. Mod. Phys.* **66**, 1481–1507 (1994).
8. A. Gierer, H. Meinhardt, A theory of biological pattern formation. *Kybernetik* **12**, 30–39 (1972).
9. I. Prigogine, G. Nicolis, On symmetry-breaking instabilities in dissipative systems. *J. Chem. Phys.* **46**, 3542–3550 (1967).
10. I. Prigogine, R. Lefever, Symmetry breaking instabilities in dissipative systems. ii. *J. Chem. Phys.* **48**, 1695–1700 (1968).
11. S. T. Vittadello, T. Leyshon, D. Schnoerr, M. P. Stumpf, Turing pattern design principles and their robustness. *Philos. Trans. R. Soc. A* **379**, 20200272 (2021).
12. S. Kondo, R. Asai, A reaction–diffusion wave on the skin of the marine angelfish Pomacanthus. *Nature* **376**, 765–768 (1995).
13. S. Kondo, T. Miura, Reaction-diffusion model as a framework for understanding biological pattern formation. *Science* **329**, 1616–1620 (2010).
14. H. Meinhardt, *The Algorithmic Beauty of Sea Shells* (Springer Science & Business Media, 2009).
15. P. K. Maini, T. E. Woolley, R. E. Baker, E. A. Gaffney, S. S. Lee, Turing's model for biological pattern formation and the robustness problem. *Interface Focus* **2**, 487–496 (2012).
16. M. Fu, T. Burkart, I. Maryshev, H. G. Franquelim, A. Merino-Salomón, M. Reverte-López, E. Frey, P. Schwille, Mechanochemical feedback loop drives persistent motion of liposomes. *Nat. Phys.* **19**, 1211–1218 (2023).
17. A. R. Sanderson, R. M. Kirby, C. R. Johnson, L. Yang, Advanced reaction-diffusion models for texture synthesis. *J. Grap. Tools* **11**, 47–71 (2006).
18. B. Abécassis, C. Cottin-Bizonne, C. Ybert, A. Ajdari, L. Bocquet, Boosting migration of large particles by solute contrasts. *Nat. Mater.* **7**, 785–789 (2008).
19. I. Theurkauff, C. Cottin-Bizonne, J. Palacci, C. Ybert, L. Bocquet, Dynamic clustering in active colloidal suspensions with chemical signaling. *Phys. Rev. Lett.* **108**, 268303 (2012).
20. A. Banerjee, T. M. Squires, Long-range, selective, on-demand suspension interactions: Combining and triggering soluto-inertial beacons. *Sci. Adv.* **5**, eaax1893 (2019).
21. S. Shin, E. Um, B. Sabass, J. T. Ault, M. Rahimi, P. B. Warren, H. A. Stone, Size-dependent control of colloid transport via solute gradients in dead-end channels. *Proc. Natl. Acad. Sci.* **113**, 257–261 (2016).
22. A. Kar, T.-Y. Chiang, I. Ortiz Rivera, A. Sen, D. Velegol, Enhanced transport into and out of dead-end pores. *ACS Nano* **9**, 746–753 (2015).
23. N. Singh, G. T. Vladisavljević, F. Nadal, C. Cottin-Bizonne, C. Pirat, G. Bolognesi, Reversible trapping of colloids in microgrooved channels via diffusiophoresis under steady-state solute gradients. *Phys. Rev. Lett.* **125**, 248002 (2020).
24. A. Banerjee, I. Williams, R. N. Azevedo, M. E. Helgeson, T. M. Squires, Soluto-inertial phenomena: Designing long-range, long-lasting, surface-specific interactions in suspensions. *Proc. Natl. Acad. Sci.* **113**, 8612–8617 (2016).
25. N. Shi, R. Nery-Azevedo, A. I. Abdel-Fattah, T. M. Squires, Diffusiophoretic focusing of suspended colloids. *Phys. Rev. Lett.* **117**, 258001 (2016).
26. J. L. Wilson, S. Shim, Y. E. Yu, A. Gupta, H. A. Stone, Diffusiophoresis in multivalent electrolytes. *Langmuir* **36**, 7014–7020 (2020).
27. B. Akdeniz, J. A. Wood, R. G. Lammertink, Diffusiophoresis and diffusio-osmosis into a dead-end channel: Role of the concentration-dependence of zeta potential. *Langmuir* **39**, 2322–2332 (2023).
28. A. Gupta, S. Shim, H. A. Stone, Diffusiophoresis: from dilute to concentrated electrolytes. *Soft Matter* **16**, 6975–6984 (2020).
29. B. M. Alessio, S. Shim, A. Gupta, H. A. Stone, Diffusioosmosis-driven dispersion of colloids: A Taylor dispersion analysis with experimental validation. *J. Fluid Mech.* **942**, A23 (2022).
30. B. M. Alessio, S. Shim, E. Mintah, A. Gupta, H. A. Stone, Diffusiophoresis and diffusioosmosis in tandem: Two-dimensional particle motion in the presence of multiple electrolytes. *Phys. Rev. Flu.* **6**, 054201 (2021).
31. R. R. Raj, C. W. Shields, A. Gupta, Two-dimensional diffusiophoretic colloidal banding: Optimizing the spatial and temporal design of solute sinks and sources. *Soft Matter* **19**, 892–904 (2023).
32. K. Painter, P. Maini, H. G. Othmer, Stripe formation in juvenile Pomacanthus explained by a generalized Turing mechanism with chemotaxis. *Proc. Natl. Acad. Sci.* **96**, 5549–5554 (1999).
33. M. Yamaguchi, E. Yoshimoto, S. Kondo, Pattern regulation in the stripe of zebrafish suggests an underlying dynamic and autonomous mechanism. *Proc. Natl. Acad. Sci.* **104**, 4790–4793 (2007).
34. B. Ramm, A. Goychuk, A. Khmelinskaia, P. Blumhardt, H. Eto, K. A. Ganzinger, E. Frey, P. Schwille, A diffusiophoretic mechanism for ATP-driven transport without motor proteins. *Nat. Phys.* **17**, 850–858 (2021).
35. D. Florea, S. Musa, J. M. Huyghe, H. M. Wyss, Long-range repulsion of colloids driven by ion exchange and diffusiophoresis. *Proc. Natl. Acad. Sci.* **111**, 6554–6559 (2014).
36. S. Shin, P. B. Warren, H. A. Stone, Cleaning by surfactant gradients: Particulate removal from porous materials and the significance of rinsing in laundry detergency. *Phys. Rev. Appl.* **9**, 034012 (2018).
37. R. Fujii, The regulation of motile activity in fish chromatophores. *Pigment Cell Res.* **13**, 300–319 (2000).
38. T. L. Williams, S. L. Senft, J. Yeo, F. J. Martin-Martinez, A. M. Kuzirian, C. A. Martin, C. W. DiBona, C.-T. Chen, S. R. Dinneen, H. T. Nguyen, C. M. Gomes, J. J. C. Rosenthal, M. D. MacManes, F. Chu, M. J. Buehler, R. T. Hanlon, L. F. Deravi, Dynamic pigmentary and structural coloration within cephalopod chromatophore organs. *Nat. Commun.* **10**, 1004 (2019).
39. J. T. Bagnara, J. D. Taylor, M. E. Hadley, The dermal chromatophore unit. *J. Cell Biol.* **38**, 67–79 (1968).
40. N. J. Marshall, F. Cortesi, F. de Busserolles, U. E. Siebeck, K. L. Cheney, Colours and colour vision in reef fishes: Past, present and future research directions. *J. Fish Biol.* **95**, 5–38 (2019).
41. D. Velegol, A. Garg, R. Guha, A. Kar, M. Kumar, Origins of concentration gradients for diffusiophoresis. *Soft Matter* **12**, 4686–4703 (2016).

42. S. Shim, J. K. Nunes, G. Chen, H. A. Stone, Diffusiophoresis in the presence of a pH gradient. *Phys. Rev. Flu.* **7**, 110513 (2022).
43. J. Liu, Y. Wu, Y. Li, L. Yang, H. Wu, Q. He, Rotary biomolecular motor-powered supramolecular colloidal motor. *Advances* **9**, eabg3015 (2023).
44. H. Kawauchi, I. Kawazoe, M. Tsubokawa, M. Kishida, B. I. Baker, Characterization of melanin-concentrating hormone in chum salmon pituitaries. *Nature* **305**, 321–323 (1983).
45. A. Gupta, B. Rallabandi, H. A. Stone, Diffusiophoretic and diffusioosmotic velocities for mixtures of valence-asymmetric electrolytes. *Phys. Rev. Flu.* **4**, 043702 (2019).
46. B. Peña, C. Pérez-García, Stability of Turing patterns in the Brusselator model. *Phys. Rev. E* **64**, 056213 (2001).
47. A. Dukhin, Z. Ulberg, V. Karamushka, T. Gruzina, Peculiarities of live cells' interaction with micro- and nanoparticles. *Adv. Colloid Interface Sci.* **159**, 60–71 (2010).
48. M. Pelz, M. J. Ward, Symmetry-breaking bifurcations for compartmental reaction kinetics coupled by two bulk diffusing species with comparable diffusivities in 2-D. *Front. Appli. Mathem. Stat.* **9**, 1110497 (2023).
49. S. Huang, I. Ernberg, S. Kauffman, Cancer attractors: A systems view of tumors from a gene network dynamics and developmental perspective. *Sem. Cell Dev. Biol.* **20**, 869–876 (2009).
50. A. Uthamacumaran, Cancer: A turbulence problem. *Neoplasia* **22**, 759–769 (2020).
51. L. Menou, C. Luo, D. Zwicker, Physical interactions in non-ideal fluids promote Turing patterns. *J. Royal S. Interface* **20**, 20230244 (2023).
52. S. Riva, L. Banetta, A. Zaccone, Solution to the two-body Smoluchowski equation with shear flow for charge-stabilized colloids at low to moderate Péclet numbers. *Phys. Rev. E* **105**, 054606 (2022).
53. A. Zaccone, Explicit analytical solution for random close packing in d= 2 and d= 3. *Phys. Rev. Lett.* **128**, 028002 (2022).
54. V. S. Doan, D.-O. Kim, C. Snoeyink, Y. Sun, S. Shin, Shape- and orientation-dependent diffusiophoresis of colloidal ellipsoids. *Phys. Rev. E* **107**, L052602 (2023).
55. A. E. Frankel, A. S. Khair, Dynamics of a self-diffusiophoretic particle in shear flow. *Phys. Rev. E* **90**, 013030 (2014).
56. J.-M. Armengol-Collado, L. N. Carenza, J. Eckert, D. Krommydas, L. Giomi, Epithelia are multiscale active liquid crystals. *Nat. Phys.*, (2023).
57. S. Popinet, Basilisk (2013–2022); http://basilisk.fr.
58. A. Yochelis, Y. Tintut, L. Demer, A. Garfinkel, The formation of labyrinths, spots and stripe patterns in a biochemical approach to cardiovascular calcification. *New J. Phys.* **10**, 055002 (2008).

Acknowledgments: We thank the Birch Aquarium at the Scripps Institution of Oceanography for providing high-resolution photographs of *A. ornata*. We thank A. Banerjee, R. R. Raj, J. G. Santiago, D. K. Schwartz, H. A. Stone, K. H. Jensen, and A. G. Rajan for helpful feedback on the manuscript. **Funding:** This work was supported by the NSF (CBET, 2238412) CAREER award and the American Chemical Society Petroleum Research Fund (65836, DNI9) Doctoral New Investigator award. **Author contributions:** Conceptualization: B.M.A. and A.G. Methodology: B.M.A. and A.G. Investigation: B.M.A. and A.G. Visualization: B.M.A. and A.G. Supervision: A.G. Writing: B.M.A. and A.G. **Competing interests:** The authors declare that they have no competing interests. **Data and materials availability:** All data needed to evaluate the conclusions in the paper are present in the paper and/or the Supplementary Materials. The code required for this study is available on Zenodo: 10.5281/zenodo.8352397.

Submitted 14 June 2023
Accepted 6 October 2023
Published 8 November 2023
10.1126/sciadv.adj2457